Beyond Barnwell: Applying lessons learned from the Barnwell site to other historic underground nuclear tests at Pahute Mesa to understand radioactive gas-seepage observations

S. Michelle Bourret [a],[*], Edward M. Kwicklis [a], Dylan R. Harp [a], John P. Ortiz [b], Philip H. Stauffer [a]

[a] Computational Earth Science, Earth and Environmental Sciences Division, Los Alamos National Laboratory, Los Alamos, NM, 87545, USA
[b] Department of Environmental Health & Engineering, John Hopkins University, Baltimore, MD, 21218, USA

ABSTRACT

An underground nuclear explosion (UNE) generates radioactive gases that can be transported through fractures to the ground surface over timescales of hours to months. If detected, the presence of particular short-lived radionuclides in the gas can provide strong evidence that a recent UNE has occurred. By drawing comparisons between sixteen similar historical U.S. UNEs where radioactive gas was or was not detected, we identified factors that control the occurrence and timing of breakthrough at the ground surface. The factors that we evaluated include the post-test atmospheric conditions, local geology, and surface geology at the UNE sites. The UNEs, all located on Pahute Mesa on the Nevada National Security Site (NNSS), had the same announced yield range (20–150 kt), similar burial depths in the unsaturated zone, and were designed and performed by the same organization during the mid-to-late 1980s. Results of the analysis indicate that breakthrough at the ground surface is largely controlled by a combination of the post-UNE barometric pressure changes in the months following the UNE, and the volume of air-filled pore space above the UNE. Conceptually simplified numerical models of each of the 16 historical UNEs that include these factors successfully predict the occurrence (5 of the UNEs) or lack of occurrence (remaining 11 UNEs) of post-UNE gas seepage to the ground surface. However, the data analysis and modeling indicates that estimates of the meteorological conditions and of the post-UNE, site-specific subsurface environment including air-filled porosity, in combination, may be necessary to successfully predict late-time detectable gas breakthrough for a suspected UNE site.

1. Introduction

1.1. History of testing and containment of UNEs at NNSS

Underground nuclear explosions (UNEs) were performed at the Nevada National Security Site (NNSS), formerly the Nevada Test Site (NTS), between 1957 and 1992 when the U.S. unilaterally imposed a moratorium on nuclear testing (U.S. DOE, 2015). Containment of UNE-generated gases in the subsurface was a major goal during testing to reduce the risk of transport in the atmosphere and subsequent radioactive fallout (U.S. Congress, 1989). Despite careful experimental planning and design, between 1963 when the Limited Test Ban Treaty (LTBT) banning atmospheric tests went into effect and 1992 when the US testing program ended, 105 of the 733 post-LTBT UNEs at the NNSS produced radioactive gases at the ground surface. Gases were the result of prompt release (0–2 days), either by containment failure and operation releases, or late-time gas seepage (>2 days, and up to several months) following the UNE test date (Schoengold et al., 1996; Kalinowski, 2011). The radiation released between 1970 and 1989 from testing resulted in relatively modest radiation releases in the

atmosphere, increasing the cumulative exposure at the NNSS boundary by the equivalent of only 1/1000 of a chest x-ray (U.S. Congress, 1989). Although the impact of radioactive gas released by these UNEs to the atmosphere is small with respect to human health risk, detection of short-lived gaseous radionuclides from a suspected site can provide clear evidence of recent underground nuclear testing (Carrigan et al., 1996; Kalinowski et al., 2010), and thus is of interest from a national security perspective. The history of radionuclide releases at the NNSS demonstrates that atmospheric releases of radioactivity are likely, even by experienced testing organizations with a strong motivation to prevent such releases. Furthermore, based on data from Schoengold et al. (1996), Kalinowski et al. (2010) concluded that there is no obvious depth-to-explosive-yield ratio above which containment of radioactive gases is always achieved, nor is there a strong relation between the total release activity and depth of burial.

This paper focuses on one release mechanism – the release of radionuclides from barometrically-driven, late-time seepage. This paper uses the term *late-time seepage* to describe the arrival of radioactive gases at the ground surface at concentration above 1 mBq/m^3 based on detection limit of 0.58 mBq/m^3 from Dresel and Waichler (2004). Unlike

---

uncontrolled releases from containment failure, which follow within minutes to hours after an UNE, or operational releases, which typically follow within days to a few weeks after an UNE (Kalinowski et al., 2010), late-time seepage due to barometric pumping has a more broad release window due to uncertainty in the many factors that influence it (Jordan et al., 2014). Moreover, whereas uncontrolled and operational releases have release durations of minutes to tens of hours, late-time seepage can persist for months.

This study is the first to investigate details of the post-UNE gas seepage histories for 16 moderate yield (20–150 kt) UNEs with similar burial depths (475–675 m below ground surface - bgs) conducted by a single organization, Lawrence Livermore National Laboratory (LLNL), during the mid-to-late 1980s in volcanic rocks in the deep unsaturated zone. All 16 UNEs were done at Pahute Mesa, located in the northern portion of the NNSS, where 85 UNEs were conducted between 1965 and 1992 (U.S. DOE, 2015). Since 1970, late-time seepage has been a rare event, with surface detection at only 5 UNE sites at the NNSS (Kappeli, Tierra, Labquark, Bodie, and Barnwell), all of which are included in the 16 tests investigated in this study. These tests were chosen to minimize the impacts of variability in containment designs and post-UNE gas sampling strategies, which evolved over time and differed between testing organizations.

Radioactive gas activities were measured over periods ranging from days to years by noble gas samplers, located around surface ground zero (SGZ) of each test site (Woodward, 1987; Schoengold et al., 1996). However, although all 16 UNEs in the study had similar design attributes (announced yield range and depth of burial), only 5 had late-time seepage observed, raising questions as to what controls the variability in seepage outcomes. Taking advantage of available historical datasets for the 16 UNEs, factors have been identified that may explain why late-time seepage was observed following some UNEs while others were successfully contained. Identifying and studying these factors, such as characteristics of the barometric pressure records around the UNE date, surface and subsurface hydrogeological conditions, surface damage, and air-filled porosity above the working point (location of detonation), will help in analyzing the potential for post-UNE late-time seepage at suspected foreign sites, where general knowledge of site-specific meteorological and subsurface geologic data may be available.

1.2. Gases around UNEs

UNEs produce radioactive gases around the working point that can migrate over short and long time-scales, and may potentially reach the ground surface (Carrigan and Sun, 2012). Gas seepage is controlled by advective and diffusive transport, and arrival time at the ground surface depends on many variables, including rock and fracture properties, detonation yield, depth of burial, water content, barometric pressure history, and gas transport properties (Carrigan et al., 1997, 2016; Jordan et al., 2014, 2015; Bourret et al., 2019). In addition to producing radioactive gases, the detonation of an UNE will damage the subsurface around the working point, with damage potentially reaching the ground surface. An UNE can create 1) an underground void or cavity caused by vaporization and mechanical compression of the nearby rock, 2) an overlying-rubblized column of rock referred to as a chimney that forms when rock collapses into the cavity, and 3) explosion-induced fractures around the working point (Fig. 1). The UNE-damage structure may interact with and link together with pre-existing fractures and faults to form a continuous transport pathway to the surface. However, there is evidence for decrease in permeability in the damage zones beyond the cavity due to pore compression (Bear and Corapcioglu, 1991), but in
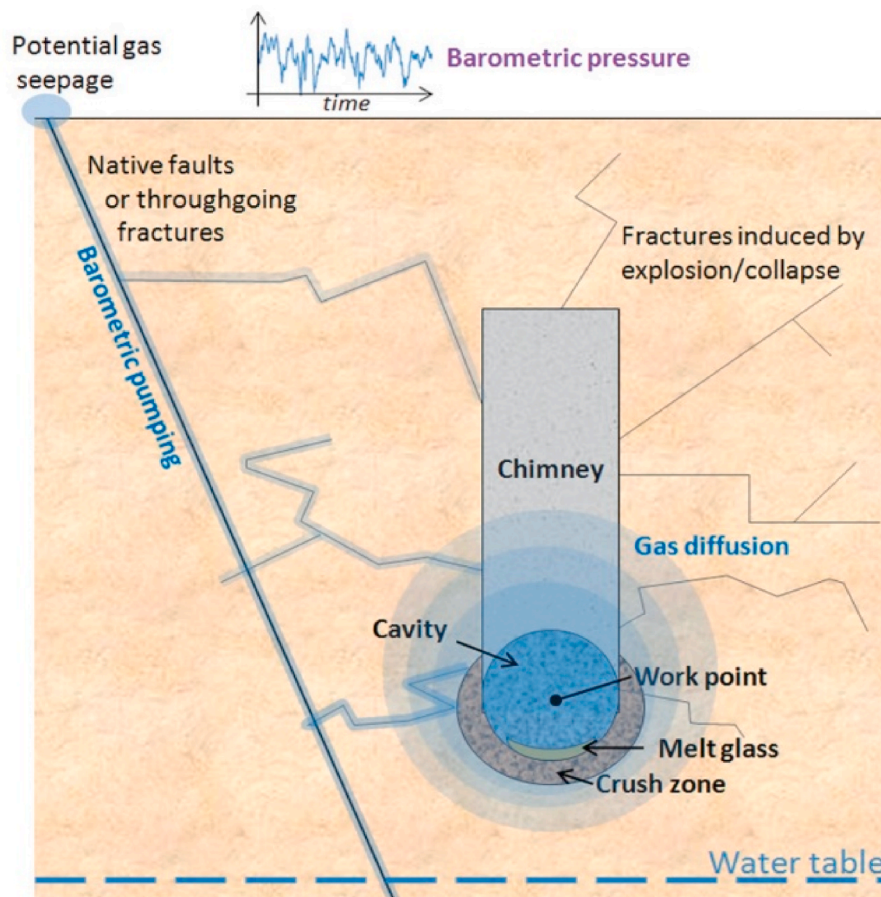

Fig. 1. Conceptualization of subsurface damage and gas migration pathways to the ground surface by barometric pumping after an UNE (from Jordan et al., 2014).

hard, brittle rocks new fractures form that may enhance permeability. This study assumes UNE damage zones are areas of increased fracturing and permeability.

UNE-related subsurface gases can migrate through preferential pathways including the stemming column, pre-existing fractures, and hydraulic fractures created by high initial gas pressures (Burkhard et al., 1989). During early time (seconds to days), gas flow is driven by over-pressure and heat-generated convection from the UNE (Sun and Carrigan, 2014). However, late-time gas seepage during the weeks to months after the explosion is driven by barometric pumping (Carrigan et al., 1996; Lowrey et al., 2013) after initial high temperature and pressure have dissipated. With barometric pumping, air flows into and out of the unsaturated zone during atmospheric pressure highs and lows, respectively, with gases stored in the subsurface pulled toward the ground surface during barometric pressure lows and pushed into the subsurface during barometric pressure highs (Auer et al., 1996; Scanlon et al., 2001; Massmann and Farrier, 1992; Neeper, 2002; Neeper and Stauffer, 2005, 2012; Harp et al., 2019). In fractured porous media, including many of the volcanic rocks at Pahute Mesa, gas flow is primarily through large aperture (i.e. high permeability) interconnected fractures. The rock matrix has much lower pneumatic diffusivity and acts primarily to store gases during their upward migration through the fracture network. Based on numerical experiments, diffusion of gas from the fractures into the rock matrix and its dissolution and subsequent release from the pore back into the fracture water may either accentuate or delay upward transport of the gases, depending on the water saturation, estimated matrix gas diffusion coefficients, and rates of pore-water dissolution (Harp et al., 2018, 2019). Asymmetry in the vertical displacement of gases during rising and falling barometric pressure cycles due to matrix diffusion and no-flow gas boundary conditions at the water table or basement rock results in an upward net displacement of gases (Nilson et al., 1991 a,b; Carrigan et al., 1996; Neeper and Stauffer, 2005; Carrigan et al., 2016; Harp et al., 2019).

Burkhard et al. (1989) discuss several ways that gas transport is dependent on properties of the rock type in which an UNE is detonated - in particular, the permeability of the background rock and the fracture properties, both pre-existing and explosion-induced. A few large-aperture, vertical fractures in a low-permeability block will be more likely to transport gases to the ground surface quickly than if more abundant, minor fractures are present. This difference in gas transport behavior is due to how the fracture and matrix properties affect pneumatic diffusivity and fracture/matrix gas exchange in fractured rock. Additionally, a higher-permeability matrix allows for greater air flow into available pore spaces and will slow upward gas migration through fractures.

Pneumatic diffusivity controls the attenuation and phase lag of a subsurface pressure signal, and depends on the ratio of gas permeability to gas storage:

$$\alpha = \frac{k_a p_o}{\mu_a \theta_a} \qquad (1)$$

where α is the pneumatic diffusivity (m^2/s), k_a is the effective air permeability (m^2), p_o is the average gas pressure (Pa), μ_a is the dynamic viscosity of air (Pa·s), and θ_a is air-filled porosity (-). Fractures in volcanic rocks tend to have diffusivities 1 to 3 orders of magnitude higher than the adjacent matrix (Burkhard et al., 1989; Bourret et al., 2019), and thus provide a much more effective pathway for gas flow. The UNE-damage structure also changes the pneumatic diffusivity, and may even improve the likelihood of gas containment, depending on chimney properties. Peterson et al. (1977a,b; 1978) conducted air-injection and tracer tests in several cavity/chimney systems of UNEs in volcanic rocks at the NNSS, which includes many of the same hydrostratigraphic units (HSUs) associated with the 16 UNE sites chosen for this study. Their results showed that the chimney had both a high permeability (10^{-12} to 10^{-11} m^2) as well as a high air-filled porosity (5–12%) relative to most of the surrounding rocks. According to eq. (1), the higher permeability and porosity created by the collapse of the chimney affect the pneumatic diffusivity, and thus the barometric pumping efficiency, in opposite ways. The large air-filled porosity of the chimney acts to slow upward gas migration whereas the high permeability of the chimney acts to accelerate upward gas migration. Similar relationships hold for the rock matrix and fractures in other model layers and damage zones, and it is important to bracket their possible ranges when estimating the potential for late-time seepage.

1.3. UNE gas migration modeling

Gas migration models have been developed to simulate the effect of barometric pumping and UNE late-time seepage using both two-dimensional (2D - Carrigan et al., 1996; Sun and Carrigan, 2014; Jordan et al., 2015; Carrigan et al., 2016) and three-dimensional (3D) formulations (Mourzenko et al., 2014; Bourret et al., 2019). Carrigan et al. (2016) included early-time UNE-related physics, such as thermal convection and phase changes due to the heat of detonation. Bourret et al. (2019) performed modeling of field-scale gas migration in a 3D, two-phase system at the Barnwell UNE site to test the impact of topography and asymmetric geologic structure on late-time seepage in the presence of a simplified UNE damage structure. Using data sets from post-UNE experiments and site-characterization, the Bourret et al. (2019) Barnwell model was able to successfully reproduce experimental observations of gas seepage from tracer injection tests (Olsen et al., 2016) as well as the late-time seepage following the actual Barnwell UNE in 1989. Of particular significance to the present work is the fact that a high degree of agreement was achieved by Bourret et al. (2019) between simulated and observed late-time seepage associated with the Barnwell event using barometric pressure variation alone to drive gas flow. The fact that it was not necessary to invoke high temperature and pressure conditions to successfully model the post-UNE seepage observations at Barnwell led us apply this simplification to the other Pahute Mesa UNEs considered in this paper.

1.4. Study objectives

Fig. 2 shows a map of Pahute Mesa including the 16 UNEs discussed in this paper. As previously mentioned, despite the overall similarities of the UNE environments, only 5 of the 16 UNEs produced late-time seepage around SGZ, as reported in gas seepage summaries taken from a compilation of all UNE-related gas releases published by the U.S. Department of Energy (Schoengold et al., 1996). Table 1 lists UNE attributes. Given the concordance between predicted and observed late-time seepage at the Barnwell site with only barometric pressure as the driving mechanism, simplified flow and transport models were created for 15 other Pahute Mesa sites, in addition to the Barnwell site, to determine if the conclusions drawn from the intensively-studied Barnwell site (Olsen et al., 2016; Bourret et al., 2019) can be extrapolated to other UNE sites in similar hydrogeologic settings, but with simpler models that include less site-specific information. Because this group of UNEs have the same announced yield range, we assume that similar high-temperature and high-pressure conditions were present following each UNE, and therefore not a discriminator of why some UNEs experienced post-test gas seepage while others did not. Detailed modeling of the full Barnwell site (Bourret et al., 2019) suggests that a combination of seasonal barometric pressure characteristics and differences in geology can explain where and when post-UNE gas seepage occurred. This hypothesis is explored by analyzing several datasets described later and performing 2D-radial numerical gas flow and transport modeling. Using the available datasets and simulations, factors were identified that hinder or promote late-time seepage at each of the 16 UNEs. Although detailed datasets may not be available for foreign sites, remotely sourced information about geologic structure and units, or observable surface damage might be used to inform gas breakthrough
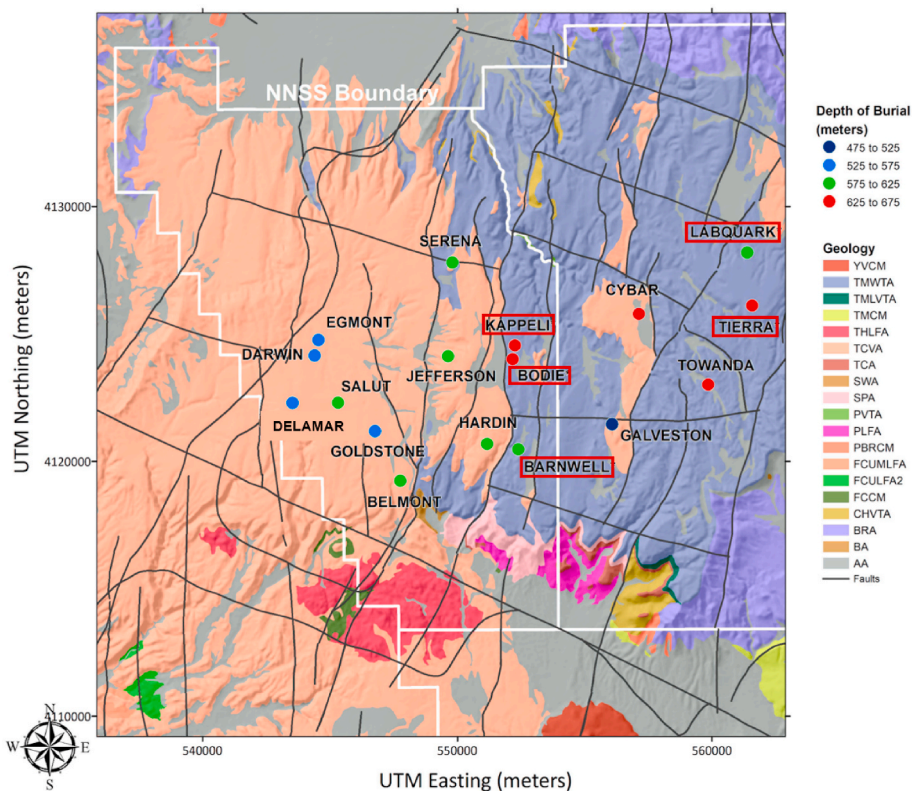
Fig. 2. Map of the surficial hydrostratigraphy of Pahute Mesa (NSTec, 2014) with UNE locations color-coded by the depth of burial. Black lines indicate faults and white lines indicate NNSS boundaries and operational areas 20 (left) and 19 (right). Red boxes indicate UNEs where seepage was observed. (For interpretation of the references to color in this figure legend, the reader is referred to the Web version of this article.)

predictions. Additionally, the use of historical or synthetic barometric pressure conditions may be used to drive gas migration models, a method previously shown to work for simple gas migration models (Harp et al., 2019).

2. Methods and datasets

Several historical datasets were used in this study including (1) surface damage maps following the UNEs; (2) surficial geology and proximity of SGZ to nearby faults; (3) pre- and post-test barometric pressure records; (4) characterization of the physical and hydrologic parameters from pre-UNE core taken from the emplacement holes.

2.1. Analysis of post-UNE surface damage

Following each UNE, a surface damage map was created that recorded new fractures and faults, fault displacement, and the creation of subsidence craters and pressure ridges. These surface damage maps were compiled and digitized by Grasso (2001) for Pahute Mesa and examined as part of this study to determine if surface damage was a possible discriminator of why some UNEs exhibited late-time seepage and others were contained. The surface damage maps for each UNE were rated on a scale of 0 (no surface damage) to 5 (severe surface damage) to see if the severity of surface damage was an indicator of post-test seepage. Criteria for assigning a given damage severity ranking are given in Table 2 and examples are given in Fig. 3. As indicated in Table 1, there is no clear relationship between late-time seepage and damage severity.

2.2. Analysis of fault proximity

By virtue of their vertical continuity, faults provide potential pathways from deeply buried UNEs to the ground surface. In general, it would be expected that longer trace length faults, such as those included in the map of the surface geology in Fig. 2, would also extend deeper. Prothro et al. (2009a) notes that faults at the NNSS have an internal architecture consisting of a slip plane, often containing a brecciated gouge zone, surrounded by a damage zone of higher fracture intensity that grades back with increasing distance from the slip plane to the background fracture intensity. In the Non-Proliferation Experiment (NPE) performed at the NNSS in the early 1990s, Carrigan et al. (1996) found that the earliest and highest tracer concentrations at ground surface following a 1 kt chemical explosion were measured along pre-existing faults at distances up to 600 m from the tracer release point. These observations, along with the results of the detailed Barnwell model of Bourret et al. (2019) that showed preferential tracer movement toward a nearby fault, suggest that proximity to faults might be affecting whether or not an individual UNE results in late-time seepage. Unfortunately, gas sampling post-UNE and following tracer injection experiments at Barnwell were concentrated around SGZ and did not include measurements from the fault areas, so this hypothesis could not be evaluated at Barnwell. Based on this reasoning, we calculated the distance from SGZ of each UNE to the nearest mapped fault feature (Table 1). Fault locations are based on a hydrostratigraphic framework model (HFM) developed by NSTec (2014). As tabulated, proximity to major faults is not an obvious factor affecting whether or not late-time seepage occurred. Although Kappeli, Bodie and Barnwell are each less than 425 m from any major faults and experienced late-time seepage, Labquark and Tierra are more than 800 m from a major fault and also experienced late-time seepage. Conversely, Serena is less than 200 m from a major fault and had no observed late-time seepage. This analysis assumes that each fault feature has a similar damage zone width and permeability, regardless of whether it is a normal fault, caldera boundary, or a vaguely defined "structural zone" identified from

Table 1

UNE information (name, date, and elevation), surficial damage rating, distance from fault, observed seepage data, h-value (air-summed filled porosity), largest pressure change within the 90 days following UNE (ΔP_{90}), $\Delta P_{90}/h$, and simulated results of late-time gas seepage for each of the 16 Pahute Mesa tests.

Event	Hole	Date	working point elevation (m)	depth of burial (m)	maximum yield (kt TNT)	water table elevation (m)	Surface Damage	Distance from Fault (m)	Surface Member	Favorable geology?	favorable barometric pressure?	Seepage Expected?	Seepage Observed?
KAPPELI	U20am	7/25/1984	1370	640	150	1356.7	1	377	TM-WTA	yes	maybe	yes	yes
EGMONT	U20al	12/9/1984	1321	546	150	1272.5	4	818	TCVA	no	yes	no	no
TIERRA	U19ac	12/15/1984	1505	640	150	1453.6	0	1333	TM-WTA	yes	yes	yes	yes
TOWNDA	U19ab	5/2/1985	1447	665	150	1420.4	1	981	TM-WTA	yes	no	no	no
SALUT	U20ak	6/12/1985	1292	608	150	1278	3	1870	TCVA	no	no	no	no
SERENA	U20an	7/25/1985	1373	597	150	1362.8	1	44	TM-WTA	yes	yes	no	no
GOLDSTONE	U20ao	12/28/1985	1370	549	150	1277.1	2	659	TCVA	no	yes	no	no
JEFFERSON	U20ai	4/22/1986	1373	609	150	1356.7	2	872	TCVA	no	no	no	no
DARWIN	U20aq	6/25/1986	1327	549	150	1274.1	4	986	TCVA	no	no	no	no
CYBAR	U19ar	7/17/1986	1416	628	119	1398.1	2	507	TCVA	no	no	no	no
LABQUARK	U19an	9/30/1986	1511	616	150	1435.3	1	833	TM-WTA	yes	yes	yes	yes
BELMONT	U20as	10/16/1986	1293	605	150	1284.4	3	573	TCVA	no	no	no	no
BODIE	U20ap	12/13/1986	1383	635	150	1356.1	2	254	TM-WTA	yes	yes	Yes	yes
DELAMAR	U20at	4/18/1987	1358	544	150	1278.6	5	1168	TCVA	no	no	no	no
HARDIN	U20ay	4/30/1987	1345	625	150	1337.8	4	765	TCVA	no	no	no	no
BARNWELL	U20az	12/8/1989	1458	600	150	1344.8	1	424	TM-WTA	yes	yes	yes	yes

Event	h - air column thickness (m)	Max pressure decrease in 90 days - ΔP^{90} (kPa)	day ΔP^{90} observed	$\Delta P^{90}/h$	Radionuclides	Seepage Period	Day of first arrival since UNE	Day of simulated arrival at SGZ since UNE
KAPPELI	76.1	2.2	56	0.029	^{85}Kr	9/24/84–7/25/86	61	34
EGMONT	84.5	2.3	13	0.027				
TIERRA	82.3	2.4	19	0.029	^{133}Xe, ^{131m}Xe, ^{85}Kr, ^{37}Ar	12/26/84–01/04/86	11	22
TOWNDA	–	1.4	11.4	–				
SALUT	116	1.2	38.1	0.01				
SERENA	61.5	2.3	71.4	0.037				
GOLDSTONE	79.2*	2.2	10.4	0.027				
JEFFERSON	90	1.9	25.4	0.021				
DARWIN	65.7	1.7	54.7	0.026				
CYBAR	–	1.7	74.5	–				
LABQUARK	94.9	3.3	25	0.035	^{133}Xe, ^{85}Kr	10/25/86–01/13/87	25	11
BELMONT	83.1	2.2	78	0.026				
BODIE	53.7	3.4	8	0.062	^{133}Xe, ^{133m}Xe, ^{131m}Xe, ^{85}Kr, ^{37}Ar	12/15/86–12/16/87	2	23
DELAMAR	85.5	1.4	34.5	0.016				
HARDIN	65.2	1.5	24	0.022				
BARNWELL	33.7	2.3	3.3	0.067	^{133}Xe, ^{133m}Xe, ^{131m}Xe, ^{85}Kr	12/17/89–03/07/90	9	9

Table 2
Surface damage severity criteria and severity score.

Score	Criteria
0	Essentially no damage
1	Minor damage (some fracturing)
2	Minor to moderate damage (more fracturing)
3	Moderate damage (substantial fracturing plus fault movement or pressure mounding)
4	Moderate to severe damage (Small collapse sink plus fault movement or pressure mounding)
5	Severe damage (Large collapse sink plus fault movement and pressure mounding)

geophysical surveys. All of these different types of features are represented in Fig. 2.

2.3. Data and analysis of barometric pressure

Historical barometric pressure data were downloaded from the Weather Underground website (https://www.wunderground.com/history) at hourly intervals between 1984 and 1990 at Mercury, NV, located just outside the southern entrance to the NNSS. Although the Mercury weather station is at a lower elevation than the average elevation of the top of Pahute Mesa, similar regional weather changes and pressure variations are present in the barometric pressure record at both Mercury and Pahute Mesa. Because it is the pressure changes, and not the absolute pressure, that drive barometric pumping, the unadjusted historical data from Mercury are adequate to compare the records following the UNEs and apply boundary conditions to the 16 gas seepage models at Pahute Mesa (see Fig. 4 for examples).

The barometric pressure record was analyzed to identify characteristics and patterns in the record that might promote high rates of subsurface gas seepage. Multi-day barometric pressure drops (~100 h) of several kPa ($\geq$0.002 MPa) have been identified as the dominant changes that drive barometric pumping, as those frequencies and amplitudes occur sufficiently often and have the potential to penetrate the subsurface to depths of the cavity and chimney where radioactive gases are present (Burkhard et al., 1989; Harp et al., 2019). The magnitude of multi-day pressure changes varies throughout the year, with larger amplitudes associated with storms during the fall and winter months, and smaller amplitudes during the spring and summer. For each UNE, the largest multi-day barometric-pressure decrease within the first 90 days following the test date was identified, and reported in Table 1 along with the day following the test that the pressure change began. These seasonal differences are evident in the barometric pressure records for the 30 days prior to and 90 days following the Bodie and Serena UNEs (Fig. 4). The Bodie UNE was detonated on Dec. 13, 1986 and the barometric pressure change amplitude is much larger than for the barometric pressure record for the Serena UNE detonated on July 25, 1985. These two barometric pressure records highlight the seasonal difference in the barometric pressure record for a UNE that has late-time seepage (Bodie)
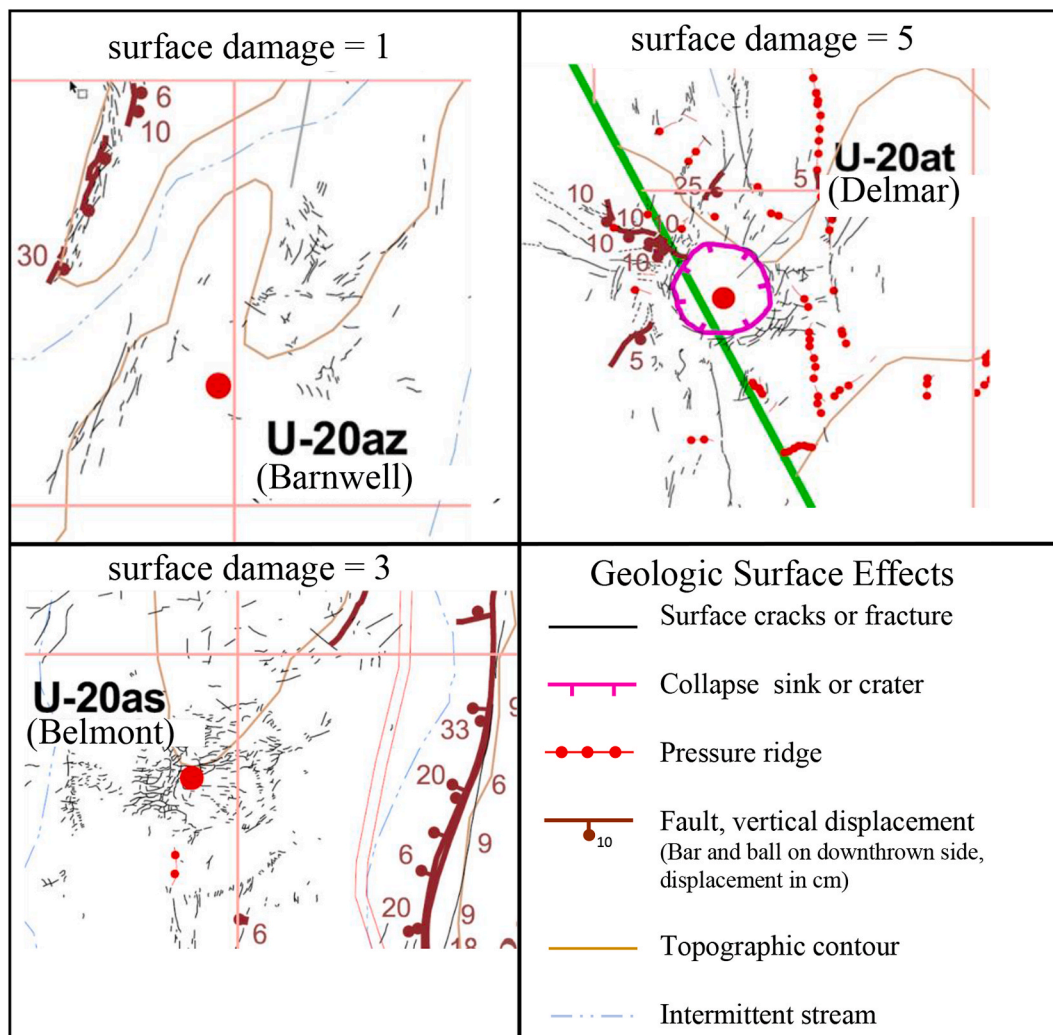

Fig. 3. Figure showing examples of surface damage severity following an UNE (modified from Grasso, 2001).
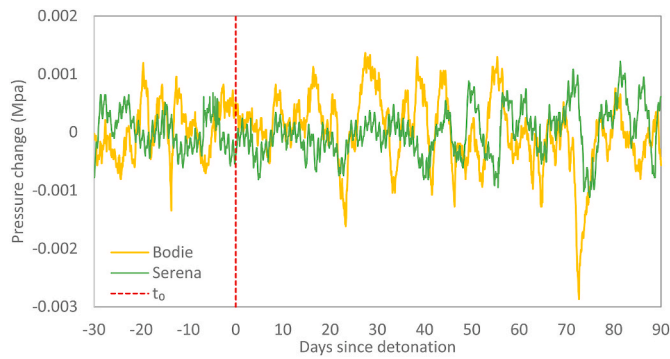
Fig. 4. Comparison of barometric pressure records for UNEs Bodie (late-time seepage detected) and Serena (contained). The vertical dashed line represents the time (t₀) of the detonation.

and a contained UNE (Serena).

2.4. Barometric pressure decomposition

In this section, we summarize an analytical barometric-pumping efficiency analysis applied to the data from the 16 UNEs presented in a companion paper, Harp et al. (2020), due to its relevance to the current research. The analytical approach is based on analytical solutions derived by Nilson et al. (1991a) and described in detail in Harp et al. (2019). The barometric-pumping efficiency quantifies the ability of a barometric component (frequency/amplitude pair) to extract gas through fractured rock to the ground surface, and we refer readers to Harp et al. (2020) for further discussion.

The barometric records collected from the Mercury, NV weather station associated with each UNE were decomposed into frequency/ amplitude pairs using a Fast Fourier Transform algorithm. As in the analysis in the previous section, the barometric records include 30 days prior and 60 days after each UNE. The top plot in Fig. 5 presents the period/amplitude pairs, where period = (2π)/frequency. The components associated with tests with late-time gas seepage to the ground surface are in red and those without seepage are in blue to indicate differences in barometric components between leaked (late-time seepage observed) and contained tests. Additional analysis of the barometric decomposition for the 16 UNEs is presented in companion paper Harp et al. (2020).
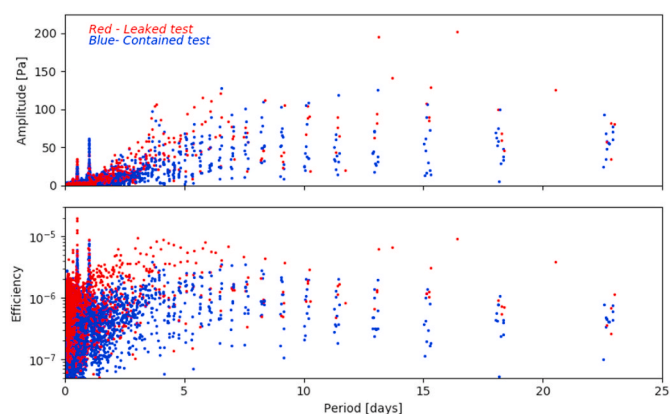
We used geologic and hydrologic data discussed below to assign air-filled porosity, matrix permeability, and depth of burial for each UNE. Using these decomposed period/amplitude pairs and properties, we then calculated the barometric pumping efficiency using equation 14 in Harp et al. (2019). We present these efficiencies in the bottom plot of Fig. 5, where the barometric components associated with leaked UNEs are in red and contained UNEs are in blue. By inspecting the locations of red versus blue points, it is apparent that for periods longer than a few days, both the amplitudes and efficiencies for leaked tests are generally higher than for contained tests.

2.5. Emplacement hole core data

Measurements from core of the emplacement holes for each of the 16 UNEs were used to estimate the hydrostratigraphy, matrix properties and pneumatic diffusivity (Wood, 2007). The core data records the undamaged, pre-UNE rock and moisture conditions. Example datasets from the Egmont and Barnwell emplacement holes (pre-shot core) are shown in Fig. 6 (Burkhard and Wagoner, 1989; Wood, 2007). The figures highlight essential differences between UNEs located in areas where the Thirsty Canyon Volcanic Aquifer (TCVA) forms the uppermost unit versus those UNEs located in areas where the Timber Mountain Welded Tuff Aquifer (TM-WTA) forms the caprock (see Table 3 for HSU descriptions). The TCVA and uppermost part of the TM-WTA typically have total porosities of approximately 40–50% and air-filled porosities averaging around 20%. Where these zones are present in the shallow subsurface, the large air-filled porosity provides storage to buffer the
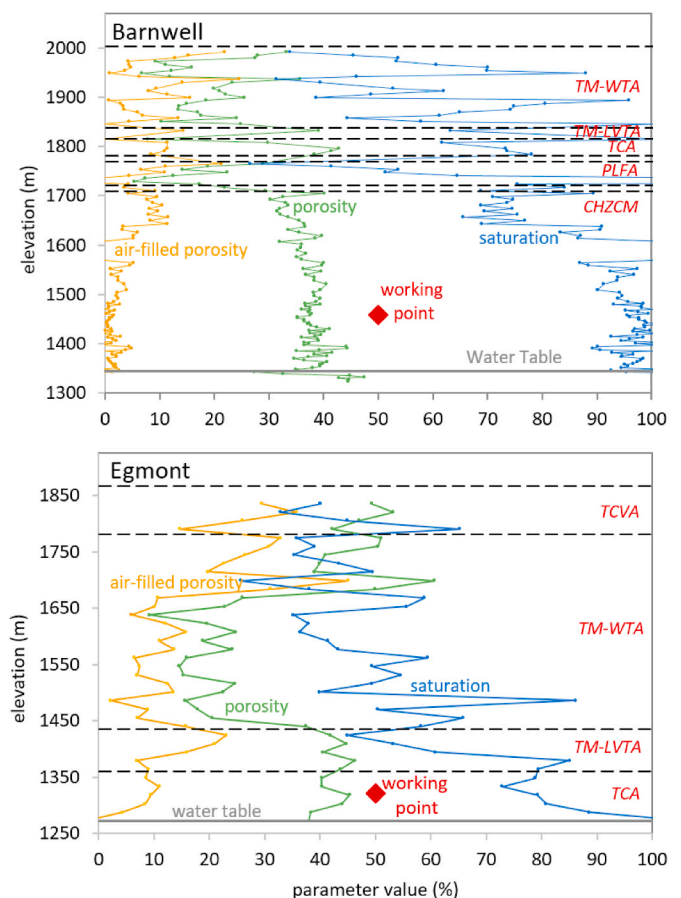

Fig. 5. (Top) Frequency decomposition of 16 barometric signals during underground nuclear tests presented as amplitudes as a function of period. (Bottom) Barometric pumping efficiency analysis of period/amplitude pairs from top plot. Red dots correspond to 5 UNEs with gas leakage at late times. Blue dots correspond to 11 contained UNEs. (From Harp et al., 2020). (For interpretation of the references to color in this figure legend, the reader is referred to the Web version of this article.)

Fig. 6. Comparison of measured saturation, porosity, and air-filled porosity from the Barnwell (top) and Egmont (bottom) emplacement holes. The elevation of the contacts between HSUs (NSTec, 2014), the water table and working points of the UNEs are also shown. Additional details for HSU depth are given on Table 3.

barometric pressure changes near ground surface, so that the pneumatic pressure changes transmitted to the working point are much weaker compared to locations where the air-filled porosity is less, as observed in the Barnwell profile. Additionally, it can be noted that non-to-partially welded tuffs with high porosity tend not to have open fractures (Prothro, 2016). Thus, thick, high air-filled porosity zones tend to reduce the likelihood that late-time seepage will occur following an UNE.

HSUs at each of the emplacement-hole locations (Fig. 6) are used to create the hydrostratigraphy for each of the 16 flow and transport models for each UNE site. The HSUs were created from the original stratigraphic designations by grouping adjacent stratigraphic units with roughly similar hydrologic and rock mechanical properties (Prothro et al., 2009b; NSTec, 2014). Air-filled porosity is determined from measurements of porosity and water saturation ($\theta_a = (1 - S) * \theta$) compiled in Wood, 2007, and can be used along with calibrated matrix permeabilities from the Barnwell site (Bourret et al., 2019) to estimate the pneumatic diffusivity of the rock matrix with eq. (1). These data were shown to be important for gas migration models following the Barnwell UNE, where model results of pressure responses at depth and tracer transport are very sensitive to the pneumatic diffusivity (Bourret et al., 2019).

In addition to populating the numerical models with subsurface porosity and saturation data, the air-filled porosity for each emplacement hole was summed above the working point to calculate the thickness of the air column (h) from the working point (wp) to the ground surface (gs) (see Fig. 6).

$$h = \sum_{wp}^{gs} \theta_{ai} * d_i \tag{2}$$

where θ_{ai} is the measured air-filled porosity in the emplacement hole multiplied by the length of the vertical interval associated with the measurement (d_i). This metric provides a measure of air-filled storage for radionuclide migration at each of the 16 UNE sites, and is presented in Table 1.

The value of h helps to explain the different late-time seepage observations at the UNE sites. For example, although Egmont has a shallower burial depth (546 m) than Barnwell (600 m), both UNEs were detonated in early December, and both experienced similar post-UNE barometric pressure drops (Table 1), Barnwell experienced late-time seepage while Egmont was contained. The absence of seepage at Egmont may be explained by its much larger air-filled column height (h = 84.5 m) compared with Barnwell (h = 33.7 m) (Table 1).

A ratio was also calculated to relate the largest pressure drops for the 90-day periods (ΔP_{90}) following the test date to h (Table 1). Although it is unlikely that a single decrease in barometric pressure is responsible for late-time seepage, ΔP_{90} provides a measure of the largest amplitude changes in the months following the UNE. The ratio ($\Delta P_{90}/h$) provides a measure of the strength of the pressure changes reaching the depth of the UNE that could draw radioactive gas to the ground surface before radioactive decay reduced the source strength of short-lived xenon isotopes to undetectable levels.

3. Numerical modeling

3.1. Model set up

The Finite Element Heat and Mass transfer code (FEHM; https://fehm.lanl.gov), a multiphase flow and transport model developed at Los Alamos National Laboratory, was used for all numerical simulations. FEHM solves the conservation of mass and momentum equations using the finite volume method (Zyvoloski, 2007; Zyvoloski et al., 2012)). Multiple studies have used FEHM for simulating gas flow and transport in the vadose zone (Stauffer et al., 2005, 2019; Kwicklis et al., 2006; Neeper and Stauffer, 2012; Jordan et al., 2014; Bourret et al., 2019). A Generalized Dual Permeability Model (GDKM) consists of two

Table 3
Depth of the top of each HSU, water table (WL), and working point (WP) at each site. A description of rock type for each HSU is included in the table.

HSU	rock type	Kappeli	Egmont	Tierra	Towanda	Salut	Serena	Goldstone	Jefferson	Darwin	Cybar	Labquark	Belmont	Bodie	Delmar	Hardin	Barnwell
TCVA	volcanic aquifer	–	0	–	–	0	–	0	0	0	0	–	–	0	–	0	–
TMWTA	welded tuff	0	85	0	0	89.9	0	82.3	56.4	100.6	78.6	0	0	89	0	71.3	0
TMLVTA	vitric tuff	158	431.6	390.1	320	356	179.2	289.6	400.5	412.7	437.7	303.3	356.6	202.7	141.5	292.3	166.1
PBPCU	tuff confining unit	–	–	–	–	436.2	–	414.5	–	–	–	–	–	303.6	–	–	–
BA	volcanic aquifer	–	–	–	–	535.8	–	472.4	–	–	–	–	–	370.9	–	–	–
UPCU	tuff confining unit	–	–	–	–	–	–	–	–	–	–	–	–	485.9	–	435.9	–
TCA	volcanic aquifer	–	506.6	440.4	358.4	–	–	–	–	490.7	495	328.9	–	–	–	–	187.5
PVTA	vitric tuff	167.6	–	448.1	374.9	–	–	–	–	–	524.6	333.1	373.9	–	–	–	222.5
PLFA	rhyolitic lava	–	–	–	399.6	–	–	–	–	–	604.1	367.6	–	–	–	–	234.7
CHVTA	vitric tuff	–	–	463.3	469.4	–	216.4	–	490.1	–	–	–	378.6	–	159.3	–	281.9
CHZCM	zeolitic tuff	286.5	–	–	–	–	–	–	–	–	–	632.2	–	–	296.6	–	295
CFCU	tuff confining unit	–	–	514.2	571.8	–	–	–	–	–	–	–	437.7	–	–	–	–
KA	alluvium	–	–	532.5	–	–	–	–	–	–	–	–	469.4	–	–	–	–
BFCU	tuff confining unit	–	–	–	637.3	–	–	–	–	–	–	–	633.4	–	–	–	–
WP elv. (m)		640.1	546.2	640.1	660.2	608.1	597.4	548.6	607.2	548.9	627.0	615.7	605.0	634.9	544.1	625.1	600.8
WL elv. (m)		652.8	594.1	691.6	691.3	622.4	606.8	636.7	625.4	601.9	646.2	674.5	691.6	613.6	662	623.4	658.7

overlapping media at each computational node, one representing fractures and one representing porous media (Jordan et al., 2012), and is applied in the model to simulate flow and transport in both matrix and fracture nodes. With the GDKM approach, fluid can move quickly through permeable, small-porosity fractures while still diffusing tracer gas into the more porous, low-permeability matrix. The GDKM approach is consistent with the conceptual models of previous investigations that consider natural and UNE-induced fractures to be the dominant pathways for gas migration due to their high permeability and small air-filled porosity (Carrigan et al., 1996, 2016; Jordan et al., 2014; Bourret et al., 2019).

Sixteen numerical models were built to evaluate gas seepage observations at deep, unsaturated-zone UNEs on Pahute Mesa. Each of the 16 sites are represented by a simple 2D-orthogonal computational mesh generated using the LANL developed software GRIDDER (https://github.com/lanl/gridder, 2018) and are solved assuming radial symmetry. The computational mesh is rectangular with radial and vertical dimensions of 500 m by 700 m, respectively. Grid spacing is uniformly 10 m in the vertical direction, and varies laterally from evenly spaced ($\Delta r = 10$ m) near the emplacement hole to logarithmically-spaced toward the outer lateral boundaries, where $\Delta r = 98$ m. Although the computational mesh is the same for all sites, the details of the emplacement hole hydrostratigraphy presented in Table 3 are assigned to distribute the flow and transport parameters for each HSU. Borehole data from NSTec (2014) was used to identify contacts between HSUs at each emplacement hole for each UNE site. Then, the average porosity, saturation, and air-filled porosity of each HSU at each emplacement hole was calculated using data compiled in Wood, 2007, and assigned to individual HSUs in each of the 16 UNE gas migration models. Permeability was assigned to the HSUs according to rock type to have consistent parameters between each site. The HSUs present at Pahute Mesa were grouped into four rock types, which include welded tuff, zeolitic tuff, vitric tuff, and rhyolitic lava. While porosity, air-filled porosity and saturation were assigned based on the emplacement-hole specific core measurements, assigning the average measured value (Fig. 6) to each HSU in each model, hydraulic properties for the fracture and matrix permeability within each of the four rock categories are assumed to be the same across the 16 models. Individual layers within each model were further assumed to be homogeneous and isotropic.

In addition, the depth of the water table and working point vary in each model. Because the measurements represent pre-shot conditions, a damage structure is overlaid on the background HSUs to represent the cavity and collapse chimney. Following the Barnwell model (Bourret et al., 2019), this inner damage zone is surrounded by an additional damage structure radiating out to 2 cavity/chimney radii to incorporate the effects of testing-induced fractures beyond the cavity and chimney. Additional damage zones between the top of the chimney and the ground surface are included to represent permeability increases associated with uplift and collapse of the ground surface due to the upward propagation of the blast wave. Properties of the damage structure zones, including porosity, fracture spacing, and permeability, are based on the calibrated damage structure parameters determined from the earlier modeling of the Barnwell site (Bourret et al., 2019). Flow parameters are reported in Table 4. An example grid for the Belmont UNE site is shown in Fig. 7.

An initial condition for each model is created by performing a simulation to establish steady-state pressure conditions at depth. Then, pre-shot conditions are simulated using the 30-day barometric pressure record prior to the UNE date to establish the transient subsurface pressure. Lastly, a radionuclide transport simulation is run using the measured barometric pressure conditions for at least 80 days, and up to 2 years following the test date for each UNE. The simulated gas activities of different radioisotopes at various distances from SGZ during this last period are recorded for comparison to the late-time seepage observations. Gas samplers and radiation detectors were deployed at each site in the mid-to-late 1980s to measure radioactive gases at the ground surface

Table 4
Parameters assigned to each HSU and damage zone, including permeability for both fracture and matrix, as well as fracture spacing. Parameters based on detailed calibration performed for the Barnwell site, described in Bourret et al. (2019).

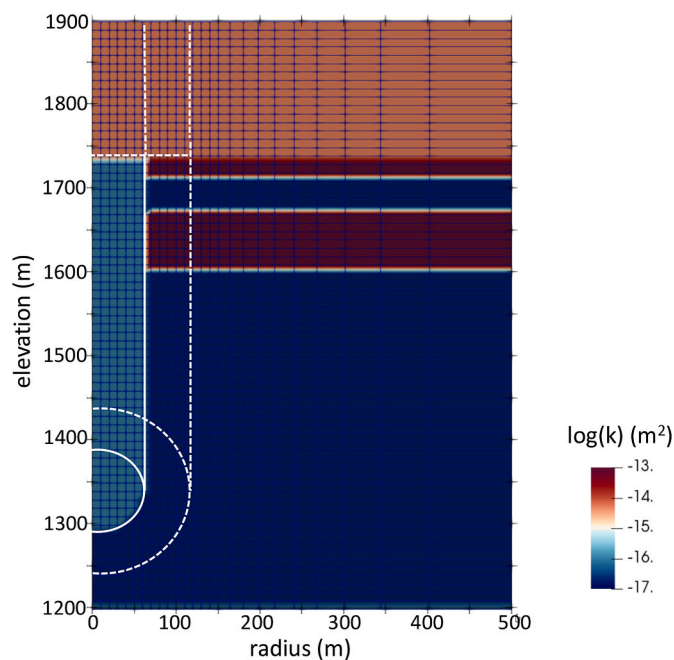| continuum	HSU	Permeability (m²)	fracture spacing (m)
matrix	rhyolitic lava	1.05e-16	–
	vitric tuff	1.44e-13	–
	welded tuff	4.14e-15	–
	zeolitic tuff	1.80e-17	–
	chimney material	1.00e-16	–
fracture	background	4e-12	1.5
	chimney/cavity (1r)	3e-10	0.5
	chimney/cavity (2r)	4e-11	1
	damage zone (1r)	8e-11	1.5
	damage zone (2r)	8e-12	1.5

Fig. 7. Example 2D computational grid used for gas migration modeling (Barnwell). The variable grid spacing (connectivity of the mesh), contacts between HSUs, and the damage zones can be seen in this figure. The different colors represent log matrix permeability, with low permeability units shown in blue, and high permeability units shown in red. (For interpretation of the references to color in this figure legend, the reader is referred to the Web version of this article.)

following the UNE. For the vertical shaft-type tests considered in this paper, the typical surface monitoring layout consisted of 8 sensors arranged in a ring centered around SGZ, as well as at SGZ itself (U.S. Congress, 1989). As mentioned elsewhere, elevated temperature and pressure conditions in the cavity and its surroundings that are generated by an UNE are not considered in these single-phase, gas flow simulations.

3.2. Transport assumptions

For computational efficiency, it is assumed that both water and gas are present in the models, but only gas is able to flow due to pressure gradients. Liquid water is precluded from moving by use of a relative permeability function that ensures virtually no liquid flux. This is an acceptable approximation for Pahute Mesa where low infiltration rates (~5 mm/yr) limit the importance of water flow for gas transport during the relatively short simulation period (80–700 days). However, the

immobile pore and fracture water participates in the transport solution by storing tracer gases through Henry's Law partitioning, and effectively slows all tracer migration to the ground surface (Neeper and Stauffer, 2012; Harp et al., 2018, 2019). Iodine, in particular, is about 800 times more soluble than xenon, and thus relatively immobile until it decays to xenon. Table 5 lists the isotope-specific half-lives, Henry's Law coefficients and free-air and free-water diffusion coefficients. The FEHM code adjusts the free-air and free-water diffusion coefficients to account for the total and air-filled porosity in both the matrix and fracture continua based on the Millington-Quirk algorithm (Millington and Quirk, 1961).

3.3. Source term

To simulate the radionuclide inventory associated with each historical UNE in an unclassified setting, an initial mass of radioactive gas is calculated using the maximum announced yield (150 kt) of each test, as listed in U.S. DOE (2015), and the moles per kt yield of individual radionuclides listed in England and Rider (1994). It is assumed that UNE-generated gases are evenly distributed in the fracture nodes of the cavity, so that the initial concentrations of individual radioactive gases in the models reflect the cavity volume and porosity. Likewise, the cavity volume itself is based on the maximum of the announced yield range in U.S. DOE (2015) and an empirical relation between cavity radius and yield, burial depth and average overburden density reported in Pawloski (1999).

The nuclear device designs and explosive yields associated with the UNEs included in this analysis are classified and unknown to the modeling team. However, to compare the different UNEs in an unclassified setting, we make the unsubstantiated assumption that explosive yield of each UNE was generated solely by fission of ^{235}U. The ^{235}U fission products from a UNE include a 133 chain starting with ^{133}In, and eventually decays to radioactive daughter products ^{133}I, ^{133m}Xe, and ^{133}Xe (Sun et al., 2014; England and Rider, 1994). By 0.1 days, ^{133}I is the dominant isotope in the 133-chain, so the moles of all parents in the 133 chain above ^{133}I produced by the fission yield are summed to find the initial masses of ^{133}I, ^{133m}Xe, and ^{133}Xe at the start of the gas transport simulation. This simplification of the decay chain reduces the computation time for the transport simulations. Simulated concentration results are reported for ^{133}Xe concentrations because it is the most abundant isotope for the time-period typical for gas detection (2–30 days). ^{85}Kr and ^{37}Ar, with half-lives of 10.7 yr and 35.04 days, are other activation product isotopes that were detected following some Pahute Mesa UNEs; however, the source terms for the 85- and 37-chains were not simulated in this study because of recent emphasis for treaty monitoring on xenon-isotopes ratios as evidence for nuclear tests (e.g. Kalinowski et al., 2010). Radioactive decay information is given in Table 5.

4. Results

4.1. Effects of air-column height and pressure drop

The $\Delta P_{90}/h$ ratios presented in Table 1 are plotted against the day the pressure drop began in Fig. 8. The $\Delta P_{90}/h$ ratios of UNEs with observed late-time seepage show a different range in values compared with the $\Delta P_{90}/h$ ratios of contained UNEs. The timing of the largest pressure swing is also a relevant variable, with four of the five tests with observed late-time seepage tending to have a large pressure swing within 30 days of detonation, before the xenon isotopes decay below their detection threshold (1 mBq/m^3). As illustrated in Fig. 8, the ratio of $\Delta P_{90}/h$ has some discriminatory power in identifying which UNEs are likely to have late-time seepage, but there is a narrow range in the $\Delta P_{90}/h$ ratio (0.3–0.4) that includes sites both with and without seepage detection at the ground surface. It should be noted, however, that after 50 days, ^{133}Xe concentrations are probably too low to be detected, given that only ^{85}Kr was detected at Kappeli at 61 days (Table 1). Therefore, the absence of detectable radionuclides for UNEs with maximum $\Delta P_{90}/h$ after 70 days at Belmont, Cybar and Serena may have as much to do with the decay of radionuclides to undetectable levels as to the $\Delta P_{90}/h$ ratio of these UNEs.

4.2. Simulation results

^{133}Xe was the dominant isotope observed during the typical late-time seepage and was thus chosen to identify if the detection limit was reached during simulation. The criterion for ^{133}Xe detection is that the simulated ^{133}Xe activity exceeds 1 mBq/m^3 at the ground surface. Other isotopes in the 133 decay chain, including ^{133m}Xe and ^{133}I have lower activities than ^{133}Xe due to differences in half-lives and branching factors on radioactive decay rates, and would be expected to be detectable only if ^{133}Xe was detected.

Table 1 shows the simulation results for each UNE. For the 5 UNEs for which late-time seepage was observed, the simulations predict gas breakthrough above the detection limit. Similarly, simulations of all contained UNEs do not show ^{133}Xe activity exceeding the detection limit at the ground surface. Although we do not directly simulate ^{37}Ar or ^{85}Kr, it is reasonable to expect that given their long half-lives (Table 5), they will eventually seep during winter months where geologic conditions are favorable. The simulations confirm that upward gas migration is highly tied to the timing of barometric pressure lows and the air-filled porosity above the working point. Although the simulations do a good job of predicting the occurrence of late-time seepage, they have variable degrees of success in predicting the timing of ^{133}Xe activity surpassing the detection limit. Typically, the late-time seepage was measured earlier than predicted by the simulation. In addition, there are several UNEs in which radioactive gases were not detected at the ground surface, but where simulated gas activities at SGZ came close to the detection limit.
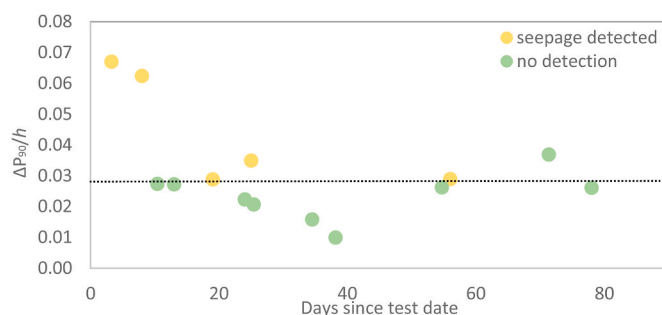
Table 5
Transport and radioactive decay parameters assigned to simulated tracers in simulations.

Transport parameter	^{133}I	^{133m}Xe	^{133}Xe
Half-life (days)	0.87	2.19	5.24
Branching factors (−)	–	0.028	0.972
Henry's Law coefficient (K_H), mol kg^{-1} bar^{-1}[a]	3.1	0.0043	0.0043
Molecular diffusion coefficient in air (D_{fa}), m^{2}s^{-1}[b]	7.20×10^{-6}	1.24×10^{-5}	1.24×10^{-5}
Molecular diffusion coefficient in water (D_w), m^{2}s^{-1}	1.2×10^{-9}[d]	1.5×10^{-9}[c]	1.5×10^{-9}[c]

[a] From Sander, 2018.
[b] From Smith and Loyalka (2010).
[c] Cantrel et al. (1997).
[d] From Carrigan et al. (1997).

Fig. 8. Ratio ($\Delta P_{90}/h$) of the largest pressure change within 90 days following each UNE (ΔP_{90}) to the thickness of the air-column above the working point (h), plotted against the day of the start of the largest pressure decrease.

The discrepancies in late-time seepage timing may be the result of the over-simplification of physical features in the subsurface. We assumed that all of the 16 UNEs had the same geometry for the cavity, chimney, and outer damage zonation. This may not be realistic when the HSU and rock mechanical properties vary, which may change the size and shape of the UNE-damage structure from UNE to UNE. The models also do not include mapped fractures, faults, or engineered features, such as the emplacement hole or other drill-back holes, where a poor seal could produce a preferential connection from the chimney to the ground surface. Additionally, the simulations do not include the heat and pressure associated with the detonation; only atmospheric pressure changes drive gas flow in the simulations. Sun and Carrigan (2014) show that the heat and pressure of detonation can be an important driver of early-time UNE-related gas flow, and ignoring this effect may be responsible for the simulated seepage arriving later than the measure seepage for Bodie, Labquark, and Tierra. Nevertheless, early-time, thermal convection is a highly energetic and localized phenomenon associated with all UNEs that is likely less affected by local variations in geology surrounding the working point than a late-time, less energetic and dispersed phenomenon such as barometric pumping, so it is not a factor that discriminates if late-time seepage or containment are likely. If these other complexities were included, it is plausible the simulations would reproduce the early detection of radioactive gases more accurately; however, we would also predict some simulated seepage that was not observed during testing using the current model set up.

Unique among the UNEs with observed late-time seepage is Kappeli, which has a favorable TM-WTA caprock, but a summer detonation date (7/24/1984). The 'quiet' barometric pressure signal immediately following this summer UNE likely limited gas flow. However, late-time seepage was observed after two months (late September) when the arrival of a fall storm resulted in a significant multi-day pressure drop. In contrast to the other UNEs with observed late-time seepage, ^{85}Kr was observed 61 days after the Kappeli detonation, and no xenon isotopes were measured. At 61 days, most of the ^{133}I, ^{133m}Xe, and ^{133}Xe isotopes would have decayed to very small activities because of their relatively short half-lives compared to ^{85}Kr (10.7 yr). The ^{85}Kr detection nearly two months after the test suggests that longer-half-life isotopes or ratios of stable daughter products may provide a longer detection window for UNEs, and should be considered in sampling strategies for suspected sites.

To illustrate the model results, Fig. 9 shows simulated results of the ^{133}Xe activity at various radial distances from SGZ for four of the UNEs: Barnwell, Bodie, Egmont, and Serena. Although the simulated ^{133}Xe activities of all UNEs increase with falling barometric pressure, as expected, the simulated ^{133}Xe activities at Barnwell and Bodie exceed the detection threshold whereas those at Egmont and Serena do not, in agreement with the observations. The results for all UNEs show that peak surface concentrations decrease with distance from SGZ, as expected for these radially-symmetric simulations.

Fig. 10 shows the simulated ^{133}Xe activities for the simplified Barnwell model at 9.3 and 50.3 days following the detonation. The simulated ^{133}Xe activities in the simplified Barnwell model are substantially different from those of the full Barnwell model (Bourret et al., 2019), despite matching the first arrival at about 10 days. Whereas the full Barnwell model that included topography, faults and lateral thinning of HSUs resulted in significant subsurface lateral transport toward a
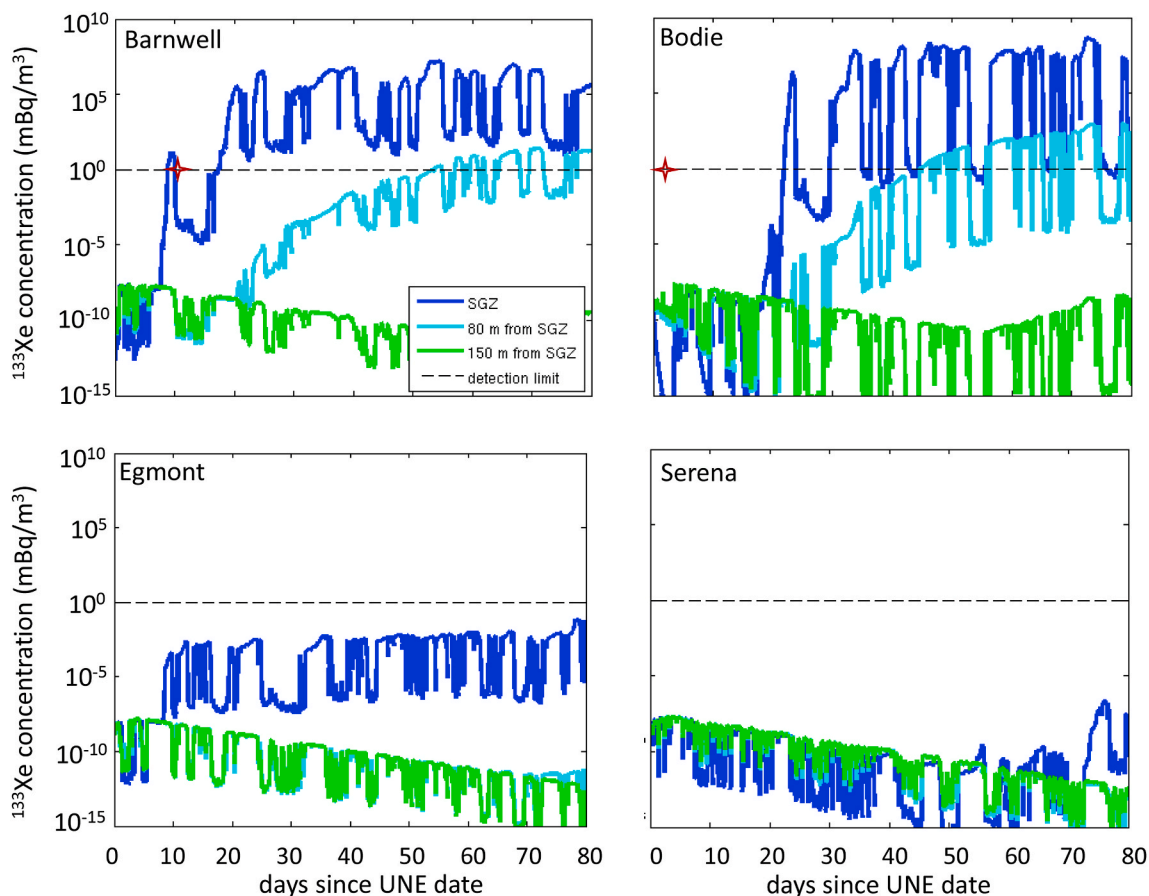

Fig. 9. Example results of simulated ^{133}Xe concentration at the ground surface relative to the detection limit: (top left) Barnwell, where late-time seepage was observed after 9 days, (top right) Bodie, where late-time seepage was observed after 2 days, (bottom left) Egmont, a contained test with unfavorable geology but favorable barometric pressure, and (bottom right) Serena, a contained UNE with favorable geology but unfavorable barometric pressure. The + indicates when seepage was observed.
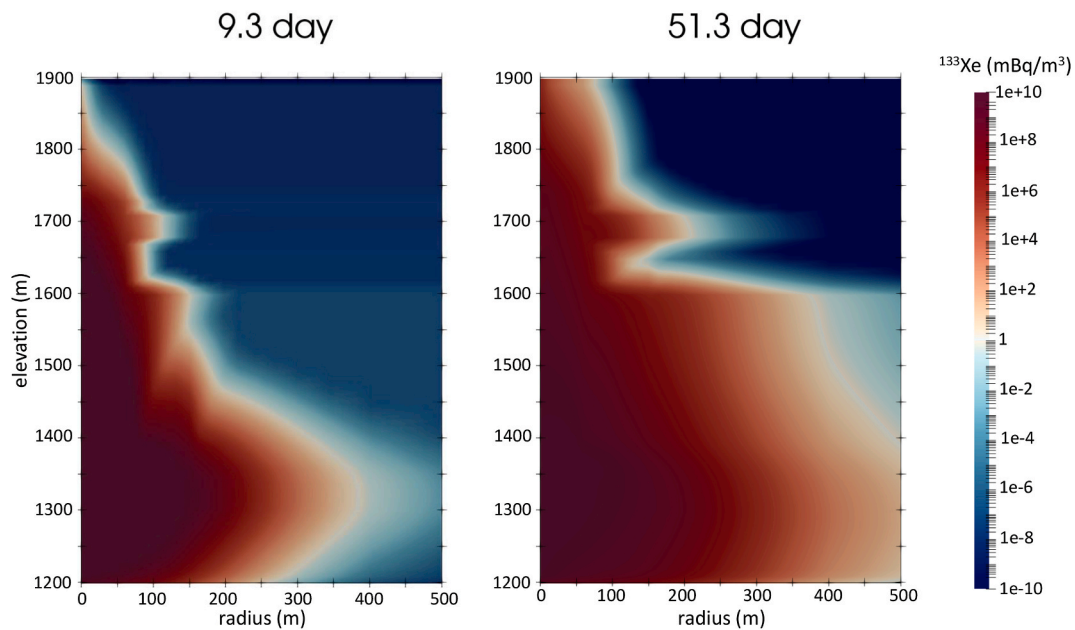
9.3 day   51.3 day

Fig. 10. Example simulated ^{133}Xe concentration (mBq/m^3) at 9.3 (left) and 51.3 days (right) following the Barnwell UNE. The detection limit is 1 mBq/m^3 (white). The influence of the damage structure on gas migration is evident in the model.

canyon as well as transport toward SGZ (Bourret et al., 2019), the simplified Barnwell model shows predominantly vertical transport centered around SGZ. The differences in seepage locations between the simplified and full Barnwell model highlight how inclusion of subsurface details impacts the location where greater late-time seepage might occur. Although the timing of the release may be more important than the seepage locations for long-range atmospheric monitoring, seepage locations may be of interest during on-site inspections.

5. Discussion

Several possible factors were considered in this study to determine what variables facilitate late-time seepage following an UNE. For the 16 Pahute Mesa UNEs examined in this study, the proximity of SGZ to the surface trace of a nearby fault and the severity of post-UNE surface damage associated with each test were not obvious factors affecting which UNEs produced late-time gas seepage and which were contained.

5.1. Mapped feature analysis

The lack of correlation between late-time seepage and the distance to nearby faults is certainly a counterintuitive result given the observations made by Bourret et al. (2019), and because large faults are likely to have deeper penetration depths and provide continuous gas transport pathways across layers with low pneumatic diffusivity. However, some faults may decrease the relative permeability of the host rock which may explain the result. It is possible that the UNEs would have to be far closer to faults than the UNEs considered in this study before radioactive gases could take advantage of enhanced fracturing in the fault damage zone, with damage zone widths of a few meters to several tens of meters observed at the NNSS (Prothro et al., 2009a; Sweetkind and Drake, 2007). It is also possible that typical monitoring strategies in the 1980s did not focus specifically on fault traces, and instead adopted a sampling strategy based on concentric rings centered on SGZ (U.S. Congress, 1989) that may have resulted in the lack of measurement of gases where and when detectable concentrations did occur. Likewise, the apparent lack of correlation between post-UNE damage severity and late-time seepage is counterintuitive. More severe surface damage that includes subsidence craters results from the upward propagation of a rubblized

chimney from the cavity all the way to ground surface. In this instance, a continuous vertical transport pathway is almost certainly present that would transport radioactive gases.

5.2. Air-filled porosity

More in line with expectations, the air-filled porosity of the host rocks overlying the working point, as well as the seasonal control on barometric pressure changes following the UNE appear to be the key factors determining whether or not radioactive gases were detected. Woodward (1987) notes that all Pahute Mesa UNEs that had late-time seepage had a welded tuff (TM-WTA) as the surficial unit. In contrast, contained UNEs had either the TM-WTA or the TCVA, as the caprock. Core data taken from the emplacement holes showed that the TCVA had consistently higher air-filled porosity than the TM-WTA. The non-to-partially welded TCVA provide ample gas storage to buffer barometric pressure changes and has few if any fractures. Both factors would tend to damp the amplitude of downward barometric changes that would draw radioactive gases upward toward the ground surface following a UNE, and therefore, the likelihood of late-time seepage. The potential for late-time seepage was vastly increased when these non-welded intervals of the TCVA and uppermost TM-WTA were eroded away, exposing the more densely-welded, fractured portions of the TM-WTA at the ground surface. However, UNEs with observed late-time seepage had TM-WTA thicknesses of 140–390 m, while UNEs without detected late-time seepage have TM-WTA thicknesses of 120–350 m, suggesting the thickness of the TM-WTA itself is not a discriminator of post-UNE seepage.

The effect of the air-filled porosity can also be seen in the decrease in the barometric efficiency. Harp et al. (2020) calculate barometric efficiencies for the 16 UNEs considered here. The results reported in their paper show that in general UNEs with late-time seepage had higher efficiencies while contained UNEs had lower efficiencies. Similarly, this result is also reflected in the $\Delta P_{90}/h$ ratios, which show higher ratios for UNEs with late-time seepage compare to contained UNEs, providing a means of discrimination based on field data. This approach relies on subsurface geologic data, which may be difficult to estimate at a suspected site; however, some basic knowledge of the geology and structure (major faults) will be available at most known or suspected UNE sites

from satellite imagery. Therefore, the porosity and perhaps even air-filled porosity could be estimated based on data from analog sites with similar material. We also expect that general information about climate and average annual precipitation of the suspected site would be known. Using data gathered remotely or from analog sites, it might be possible to estimate infiltration rates or subsurface water content.

5.3. Pahute Mesa simulations

The simulated results presented in this paper build on previous modeling and analysis at the Barnwell site, which is one of the 16 UNEs investigated in this study (see Table 1). Using the UNE-damage structure parameters estimated from previous modeling of tracer injection tests and UNE-related gas flow simulations at the Barnwell site (Bourret et al., 2019), the complexity was reduced for the 16 UNE models described in this paper, while maintaining many essential features (i.e. cavity, chimney and spall zones) necessary to predict gas seepage behavior. The results show the damage structure (chimney/cavity) had a significant control on the primary gas migration pathway, focusing flow and gas transport in the high permeability regions associated with the chimney and surrounding damage zone. However, simplifications and assumptions made in the modeling approaches of this study produced noticeably different transport patterns compared to the full Barnwell model. For example, the full Barnwell model included topography, two faults, and lateral pinching out of certain HSUs, all of which contributed to greater subsurface heterogeneity. As noted earlier, the inclusion of these features leads to significant changes in gas migration behavior compared to the simplified horizontal layering of HSUs in this study, which in contrast show gas transport up the chimney toward SGZ. Additionally, these simplified models ignore all engineered features, such as drill-back and stemming in the emplacement holes, that may provide pathways for containment failure. Thus, different seepage pathways beyond the cavity/chimney structure might be identified if faults or engineered features were included. However, the UNEs selected for this study all have similar engineered features and drill-back histories, as well as similar yield range and depth of burial, suggesting these factors are not discriminating factors for late-time seepage occurrence. We conclude that the details of the subsurface heterogeneity matter for predicting actual seepage locations, but may be less important for remote sampling where the likelihood and timing of seepage is of primary interest.

6. Conclusions

Data associated with 16 UNEs conducted at Pahute Mesa, NNSS, in the mid-to-late 1980s were examined to determine what factors control whether or not late-time seepage following a UNE was likely to occur. Five of the 16 UNEs had detectable post-UNE gas seepage in the days to months following each test, whereas the remaining 11 did not. Each of the 16 UNEs were conducted in tuffs, had similar depths of burial, explosive yield ranges, and were conducted by the same testing organization using the same emplacement and stemming methods and post-UNE gas monitoring approach. Among the possible factors examined were the degree of surface damage, proximity to faults, hydrostratigraphy, and characteristics of the barometric pressure record following the UNEs. From detailed analyses it was determined that:

1. There is no clear relationship between surface damage intensity or proximity to faults and the likelihood of late-time seepage.
2. The presence of a high porosity surface HSU (TCVA) and other subsurface HSUs with high air-filled porosity (vitric tuff) contributes to high gas storage and decreases the pneumatic diffusivity in the shallow subsurface. This damps the effect of barometric pumping and decreases the likelihood of late-time surface gas seepage.
3. The season of the test date of an UNE may be an important factor in predicting if late-time seepage will occur. At Pahute Mesa, this is due to the greater amplitudes in multi-day barometric pressure swings,

and thus a strong increase in the barometric efficiency and $\Delta P_{90}/h$ during the fall and winter months.
4. Simplified numerical models of each of the 16 UNE sites were able to reproduce the observed occurrence of late-time seepage or containment for each UNE site when they incorporated the UNE-specific hydrostratigraphy, air-filled porosity measurements, and the historical barometric pressure data at each site. However, the precise timing of detection for UNEs with late-time seepage is not currently captured in the simulation results, which can be attributed to simplified geometries and possibly the neglect of early time post-UNE pressure and temperature effects. The models presented here indicate the level of accuracy that could be expected when attempting to estimate the occurrence and timing of post-UNE seepage at foreign sites where a reasonable degree of knowledge about the subsurface and seasonal meteorological conditions exists.

Declaration of competing interest

The authors declare that they have no known competing financial interests or personal relationships that could have appeared to influence the work reported in this paper.

Acknowledgements

Appendix A. Supplementary data

Supplementary data to this article can be found online at https://doi.org/10.1016/j.jenvrad.2020.106297.

References

Auer, L.H., Rosenberg, N.D., Birdsell, K.H., Whitney, E.M., 1996. The effects of barometric pumping on contaminant transport. J. Contam. Hydrol. 24, 145–166. https://doi.org/10.1016/S0169-7722(96)00010-1.

Wave Propagation on porous media – a review. In: Bear, J.M., Corapcioglu, M.Y. (Eds.), 1991. Transport Processes in Porous Media. Kluwer Academic Publishers, pp. 373–469.

Bourret, S.M., Kwicklis, E.M., Miller, T.A., Stauffer, P.H., 2019. Evaluating the importance of barometric pumping for subsurface gas transport near an underground nuclear test site. Vadose Zone J. 18 (1) https://doi.org/10.2136/vzj2018.07.0134.

Burkhard, N.R., Wagoner, J.L., 1989. U20az Site Characteristics Report. Lawrence Livermore National Laboratory Internal Memorandum CP 89-67, April 30, 1989.

Burkhard, N.R., Hearst, J.R., Peterson, E.W., Nilson, R.H., Lie, K.H., 1989. Containment of cavity gas in fracture or rubblized emplacement media. In: The 5th Symposium on Containment of Underground Nuclear Explosions, Sept. 19-21, 1989, vol. 1. Mission Research Corp., Santa Barbara, CA, pp. 253–280.

Cantrel, L., Chaouche, R., Chopin-Dumas, J., 1997. Diffusion coefficients of molecular iodine in aqueous solutions. J. Chem. Eng. Data 42 (1), 216–220. https://doi.org/10.1021/je960178u.

Carrigan, C.R., Sun, Y., 2012. Detection of noble gas radionuclides from an underground nuclear explosion during a CTBT on-site inspection. Pure Appl. Geophys. https://doi.org/10.1007/s00024-012-0563-8.

Carrigan, C.R., Heinle, R.A., Hudson, G.B., Nitao, J.J., Zucca, J.J., 1996. Trace gas emissions on geological faults as indicators of underground nuclear testing. Nature 382, 528–531. https://doi.org/10.1038/382528a0.

Carrigan, C.R., Heinle, R.A., Hudson, G.B., Nitao, J.J., Zucca, J.J., 1997. Barometric gas transport along faults and its application to nuclear test-ban monitoring. Rep. UCRL-JC-127585. Lawrence Livermore National Lab., Livermore, CA.

Carrigan, C.R., Sun, Y., Hunter, S.L., Ruddle, D.G., Wagoner, J.L., Myers, K.B.L., Emer, D. F., Drellack, S.L., Chipman, V.D., 2016. Delayed signatures of underground nuclear explosions. Sci. Rep. https://doi.org/10.1038/srep23032M3, 2016/03/16/online 623032.

Dresel, P.E., Waichler, S.R., 2004. Evaluation of Xenon Gas Detection as a Means for Identifying Buried Transuranic Waste at the Radioactive Waste Management Complex. Rep. PNNL-14617. Idaho National Environmental and Engineering Laboratory, Pacific Northwest National Lab., Richland, WA.

England, T.R., Rider, B.F., 1994. ENDF-349 Evaluation and Compilation of Fission Product Yields 1993. Los Alamos National Laboratory, LA-UR, pp. 94–3106.

Grasso, D.N., 2001. GIS Surface Effects Archive of Underground Nuclear Detonations Conducted at Yucca Flat and Pahute Mesa, Nevada Test Site, Nevada. U.S. Geological Survey Open File Report 01-272.

Harp, D.R., Ortiz, J.P., Pandey, S., Karra, S., Anderson, D., Bradley, C., Viswanathan, H., Stauffer, P.H., 2018. Immobile pore-water storage enhancement and retardation of gas transport in fractured rock. Transport Porous Media 124 (2), 369–394.

Harp, D.R., Ortiz, J.P., Stauffer, P.H., 2019. Identification of dominant gas transport frequencies during barometric pumping of fractured rock. Sci. Rep. 9 (1), 9537.

Harp, D.R., M Bourret, S., Stauffer, P.H., Kwicklis, E.M., 2020. Discriminating underground nuclear explosions leading to late-time radionuclide gas leakage. Geophys. Res. Lett. 47, e2019GL086654 https://doi.org/10.1029/2019GL086654.

Jordan, A.B., MacCarthy, J.K., Stauffer, P.H., Zyvoloski, G.A., Person, M.A., Anderson, D. N., 2012. Simulation of radionuclide gas breakthrough from underground nuclear explosions. In: Proceedings of the 2012 Monitoring Research Review: Ground Based Nuclear Explosion Monitoring Technologies, Albuquerque, NM. 18–20 Sept. 2012, vol. 2. Natl. Nucl. Secur. Admin., Washington, DC, pp. 625–634.

Jordan, A.J., MacCarthy, J.K., Stauffer, P.H., Zyvoloski, G.A., Person, M.A., Anderson, D. N., 2014. Uncertainty in prediction of radionuclide gas migration from underground nuclear explosions. Vadose Zone J. https://doi.org/10.2136/vzj2014.06.0070.

Jordan, A.J., Stauffer, P.H., Knight, E.E., Rougier, E., Anderson, D.N., 2015. Radionuclide gas transport through nuclear explosion-generated fracture networks. Sci. Rep. 5 https://doi.org/10.1038/srep18383. Article number: 18383.

Kalinowski, M.B., 2011. Characterization of prompt and delayed atmospheric radioactivity releases from underground nuclear tests at Nevada as a function of release time. J. Environ. Radioact. 102, 824–836.

Kalinowski, M.B., Axelsson, A., Bean, M., Blanchard, X., Bowyer, T.W., Brachet, G., Hebel, S., McIntyre, J.I., Peters, J., Pistner, C., Raith, M., Ringbom, A., Saey, P., Schlosser, C., Stocki, T.J., Taffary, T., Ungar, R.K., 2010. Discrimination of nuclear explosions against civilian sources based on atmospheric xenon isotopic activity ratios. Pure Appl. Geophys. 167 (4–5), 517–539.

Kwicklis, E.M., Wolfsberg, A.V., Stauffer, P.H., Walvoord, M.A., Sully, M.J., 2006. Multiphase, multicomponent parameter estimation for liquid and vapor fluxes in deep arid systems using hydrologic data and natural environmental tracers. Vadose Zone J. https://doi.org/10.2136/vzj2006.0021.

Lowrey, J.D., Biegalski, S.R., Deinert, M.R., 2013. UTEX modeling of radioxenon isotopic fractionation resulting from subsurface transport. J. Radioanal. Nucl. Chem. 296 (1), 129–134.

Massmann, Joel, Farrier, Daniel, 1992. Effects of atmospheric pressures on gas transport in the vadose zone. Water Resour. Res. 28 (3), 777–791. https://doi.org/10.1029/91WR02766.

Millington, R.J., Quirk, J.P., 1961. Permeability of porous solids. Trans. Faraday Soc. 57, 1200–1207. https://doi.org/10.1039/tf9615701200.

Mourzenko, V.V., Varloteaux, C., Guillon, S., Thover, J.F., Pili, E., Adler, P.M., 2014. Barometric pumping of a fractured porous medium. Geophys. Res. Lett. 41 (19), 6698–6704. https://doi.org/10.1002/2014GL060865.

Neeper, D.A., 2002. Investigation of the vadose zone using barometric pressure cycles. J. Contam. Hydrol. 54, 59–80.

Neeper, D.A., Stauffer, P.H., 2005. Unidirectional gas flow in soil porosity resulting from barometric pressure cycles. J. Contam. Hydrol. 78 (4), 281–289.

Neeper, D.A., Stauffer, P.H., 2012. Transport by oscillatory flow in soils with rate-limited mass transfer: 1. Theory. Vadose Zone J. https://doi.org/10.2136/vzj2011.0093.

Nilson, R.H., Peterson, P.E., Lie, K.H., Burkhard, N.R., Hearst, J.R., 1991a. Atmospheric pumping: a mechanism causing vertical transport of contaminated gases through fractured permeable media. J. Geophys. Res. 96, 21933–21948. https://doi.org/10.1029/91JB01836.

Nilson, R.H., Lagus, P.L., McKinnis, W.B., Hearst, J.R., Burkhard, N.R., Smith, C.F., 1991b. Field measurements of tracer gas transport induced by barometric pumping. In: 6th Symposium of Containment of Underground Nuclear Explosions. Sept. 24-27, 1991, vol. 1. University of Nevada, Reno, pp. 359–375.

NSTec, 2014. Phase II Hydrostratigraphic Framework Model for Corrective Action Units 101 and 102: Central and Western Pahute Mesa, Nye County, Nevada. draft November. DOE/NV/25946-xxx.

Olsen, K.B., Kirkham, R.R., Woods, V.T., Haas, D.H., Hayes, J.C., Bowyer, T.W., et al., 2016. Noble gas migration experiment to support the detection of underground nuclear explosions. J. Radioanal. Nucl. Chem. 307, 2603–2610.

Pawloski, G.A., 1999. Development of Phenomenological Models of Underground Nuclear Tests on Pahute Mesa, Nevada Test Site—BENHAM and TYBO. Lawrence Livermore National Laboratory Report UCRL-ID-136003, Livermore, CA.

Peterson, E., Lagus, P., Lie, K., 1977a. Summary of the Dining Car Tracer-Gas Chimney Pressurization Studies. Topical Report. Systems, Science and Software, SSS-R-77-3185 Defense Nuclear Agency, April 1977.

Peterson, E., Lagus, P., Lie, K., 1977b. Summary of the Ming Blade Tracer-Gas Chimney Pressurization Studies. Topical Report. Systems, Science and Software, SSS-R-78-3535 Defense Nuclear Agency Dec 1977.

Peterson, E., Lagus, P., Lie, K., 1978. Summary of the Mighty Epic Tracer-Gas Chimney Pressurization Studies. Topical Report. Systems, Science and Software, SSS-R-78-3542 Defense Nuclear Agency Jan 1978.

Prothro, L., 2016. Fracture Analysis of the U-20az BARNWELL Test Bed Based on Data from Borehole Image Logs, National Security Technologies Report DOE/NV/25946-xxxx, Las Vegas, NV.

Prothro, L.B., Drellack Jr., S.L., Haugstad, D.N., Huckins-Gang, H.E., Townsend, M.J., 2009a. Observations on Faults and Associated Permeability Structures in Hydrogeologic Units at the Nevada Test Site. National Security Technologies, LLC, Las Vegas, NV. DOE/NV/25946–690.

Prothro, L.B., Drellack Jr., S.L., Mercadante, J.M., 2009b. A Hydrostratigraphic System for Modeling Groundwater Flow and Radionuclide Migration at the Corrective Action Unit Scale, Nevada Test Site and Surrounding Areas, Clark, Lincoln, and Nye Counties, Nevada, DOE/NV/25946–630, Las Vegas, NV.

Sander, R., 2018. Henry's Law Constants. **NIST Chemistry WebBook, NIST Standard Reference Database Number** 69. In: Linstrom, P.J., Mallard, W.G. (Eds.). National Institute of Standards and Technology, Gaithersburg MD (retrieved May 29, 2018).

Scanlon, B.R., Nicot, J.P., Massmann, J.W., 2001. Soil gas movement in unsaturated systems. In: Warrick, A.W. (Ed.), Soil Physics Companion. CRC Press, Boca Raton, FL, pp. 297–391. http://www.beg.utexas.edu/staffinfo/Scanlon_pdf/ScanlonSoilPhysComp02.pdf. (Accessed 1 June 2013).

Schoengold, C.R., DeMarre, M.E., Kirkwood, E.M., 1996. Radiological Effluents Released from U.S. Continental Tests 1961 through 1992. Bechtel Nevada, DOE/NV-317 (Rev. 1), UC-702, August 1996.

Smith, Z.M., Loyalka, S.K., 2010. Evaporation of an iodine sphere: hindered diffusion and Langmuir's conjecture. Langmuir 26 (2), 894–898. https://doi.org/10.1021/la902374t, 2010.

Stauffer, P.H., Birdsell, K.H., Witkowski, M.S., Hopkins, J.K., 2005. Vadose zone transport of 1,1,1 trichloroethane: conceptual model validation through numerical simulation. Vadose Zone J. 4, 760–773. https://doi.org/10.2136/vzj2004.0120.

Stauffer, P.H., Rahn, T., Ortiz1, J.P., Salazar, L.J., Boukalfa, H., Behar, H.R., Snyder, E.E., 2019. Evidence for high rates of gas transport in the deep subsurface. Geophysical Research. Letters 46. https://doi.org/10.1029/2019GL082394.

Sun, Y., Carrigan, C.R., 2014. Modeling noble gas transport and detection for the Comprehensive Nuclear-Test-Ban Treaty. Pure Appl. Geophys. 171, 735–750. https://doi.org/10.1007/s00024-012-0514-4.

Sun, Y., Carrigan, C.R., Hao, Y., 2014. Radioxenon production and transport from an underground nuclear detonation to ground surface. Pure Appl. Geophys. 1–23.

Sweetkind, D.S., Drake II, R.M., 2007. Characteristics of Fault Zones in Volcanic Rocks Near Yucca Flat, Nevada Test Site, Nevada, Open-File Report 2007-1293. U.S. Geological Survey, Reston, VA.

U.S. Congress, Office of Technology Assessment, 1989. The Containment of Underground Nuclear Explosions. OTA-ISC-414. U.S. Government Printing Office, Washington, D. C.. October, 1989.

U.S. Department of Energy (Us DOE), National Nuclear Security Administration Nevada Field Office, 2015. United States Nuclear Tests, July 1945 through September 1992, DOE/NV—209-Rev 16. Las Vegas, NV.

Wood, D.B., 2007. Digitally Available Interval-Specific Rock-Sample Data Compiled from Historical Records, Nevada Test Site and vicinity, Nye County, Nevada. U.S. Geological Survey Data Series 297, Reston, VA.

Woodward, E.C., 1987. Breathing on the Mesa. In: The 4th Symposium on Containment of Underground Nuclear Explosions, vol. 2. United States Air Force Academy, Colorado Springs, Colorado, pp. 285–287. Sept. 21-24, 1987.

Zyvoloski, G.A., 2007. FEHM: a control volume finite element code for simulating subsurface multi-phase multi-fluid heat and mass transfer. Rep. LA-UR-07-3359. Los Alamos Natl. Lab., Los Alamos, NM.

Zyvoloski, G.A., Robinson, B.A., Dash, Z.V., Kelkar, S., Viswanathan, H.S., Pawar, R.J., Stauffer, P.H., Miller, T.A., Chu, S., 2012. Software User's Manual (UM) for the FEHM Application Version 3.1-3.X. LA-UR-12-24493. Los Alamos National Laboratory, Los Alamos, NM.